13th International Symposium on Turbulence and Shear Flow Phenomena (TSFP13)
Montreal, Canada, June 25–28, 2024

DIRECT NUMERICAL SIMULATION OF TURBULENT FLOW THROUGH A CONCENTRIC ANNULAR SQUARE DUCT

Taylor C. Opperman, Mark S. Tachie, Bing-Chen Wang
Department of Mechanical Engineering
University of Manitoba
Winnipeg, MB, R3T 5V6, Canada
oppermat@myumanitoba.ca, tachiem@myumanitoba.ca, BingChen.Wang@umanitoba.ca

ABSTRACT

Turbulent flow through a concentric annular square duct is studied at varying Reynolds numbers of $Re_b = 3500$, 7000 and 10500 using direct numerical simulations (DNS). The Reynolds number effects on the statistical moments of the turbulence field are investigated systematically in both physical and spectral spaces. The annular configuration introduces additional complexity to the flow physics due to the presence of the convex corners of the inner duct. It is observed that the convex corners have a significant impact on the mean velocity field and wall shear stress, and promotes generation of secondary flow structures as the Reynolds number increases. It is particularly interesting to observe that the counter-rotating vortex pair commonly seen in the concave corners of a square duct vanishes at higher Reynolds numbers. The appearance of strong secondary flows drastically alters the distribution of turbulence kinentic energy (TKE) and shear stresses across the annular gap. The influence of the inner and outer ducts on the turbulence field is further examined through analyses of energy spectra of velocity fluctuations and coherent structures.

INTRODUCTION

Turbulent flow within a concentric annular square duct has many practical engineering applications such as heat exchangers and HVAC systems. Unlike two-dimensional (2-D) flow in a plane channel, turbulent duct flow is inherently three-dimensional (3-D) featuring interactions of the boundary layers developing over all eight sidewalls. Smooth square duct flow features secondary flows that manifest as four symmetric counter-rotating vortex pairs that act to draw high-momentum fluid towards the concave corners from the duct core. By contrast, the degree of complexity is significantly elevated when the square duct is made concentric with an inner (convex) and an outer (concave) duct. In such a configuration, the flow is characterized by not only the intense interaction of eight boundary layers developing over the walls of the inner and outer ducts, but also vortexes triggered by the convex and concave corners.

Prandtl (1926) was among the first to investigate turbulent flow along a streamwise cornerered channel. In this early study, it was observed that the secondary flows in the cross-stream direction were influenced by the boundary geometry, pressure gradients and turbulent stresses. As explained by Bradshaw (1987), streamwise vorticity in a square duct is produced by the anisotropy of turbulent stresses, known as Prandtl's secondary flow of the second kind, or perhaps more informatively, turbulent-stress driven secondary flow (TDSF). Turbulent flow through a single square duct has been widely studied both experimentally and numerically. Huser *et al.* (1993) conducted DNS of a fully-developed turbulent flow in a square duct and investigated the budget balance of the Reynolds shear stresses to further examine the mechanism underlying TDSFs. Their data supported the idea that TDSFs were triggered by the anisotropy of Reynolds shear stresses and the redistribution of TKE through the production and velocity-pressure gradient terms of the Reynolds stress transport equation. Xu and Pollard (2001) conducted LES to study a concentric annular duct flow and further confirmed that the origins of TDSFs along the convex corner related to the Reynolds stress anisotropy. They observed that the secondary flow structures in a concentric annular duct differed significantly from those of a smooth square duct flow. Xu and Pollard (2008) followed up their LES study using DNS with on aim of characterizing the wall scaling laws of the resolved velocity field near concave and convex corners. Recently, Wang *et al.* (2019) conducted DNS of a concentric annular square duct flow at a bulk Reynolds number of $Re_b = 6400$ (based on half the hydraulic diameter) and compared their results with those of the earlier DNS results of Xu and Pollard (2008). They showed that the secondary flow structures featured additional vortex pairs developing around the four convex corners of the inner duct in contrast to the flow going through a single smooth duct.

Not withstanding the previous contributions reviewed above, the number of high-fidelity DNS and LES studies of turbulent flow in concentric annular square ducts is rather limited in the literature and the physical mechanisms underlying the TDSFs and their impacts on turbulence statistics and coherent structures are still not well understood. In view of this knowledge gap, the current study aims to conduct a comprehensive DNS study of concentric annular duct flows using a spectra-element code. The influence of the convex and concave duct geometry on the turbulence is thoroughly examined. Furthermore, three Reynolds numbers are compared to determine the dynamics of the turbulence field and structures under different mean axial pressure gradients.

TEST CASE AND NUMERICAL ALGORITHM

Figure 1(a) illustrates the computational domain and coordinate system of a concentric annular duct flow. Here, x, y and z represent the spanwise, vertical and streamwise coordinates and the corresponding velocity components are u, v, and w, respectively. The outer square duct has dimension $D = 2\delta$ where δ is the half width of the outer duct. The length of the domain

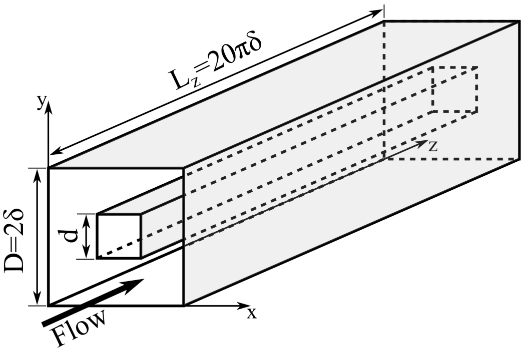

(a) Computaional domain and coordinates

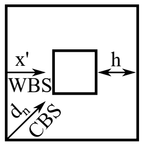

(b) Cross-sectional view

Figure 1: Computational domain and coordinate system of a concentric annular duct. The duct cross-section shows the two data extraction lines of the wall bisector (WBS) and corner bisector (CBS). The relative coordinates (x' and d_n) along the WBS and CBS have been non-dimensionalized by h.

is $L_z = 20\pi\delta$ and the ratio of the inner to outer duct width is fixed at $d/D = 1/3$. Figure 1(b) displays the two data extraction lines used in the analysis, i.e, the wall bisector (WBS) and corner bisector (CBS). The coordinates (i.e., x' and d_n) along the WBS and CBS have been non-dimensionalized by the annular gap (h) between the inner and outer ducts. Three different Reynolds numbers of $Re_b = D_h W_b/2\nu = 3500$, 7000 and 10500 are tested, where D_h, W_b, and ν denote the hydraulic diameter, bulk mean velocity, and kinematic viscosity of the fluid, respectively. It can be shown that the hydraulic diameter is $D_h = 2h = 2D/3$. The continuity and momentum equations that govern the incompressible flow read

$$\frac{\partial u_i}{\partial x_i} = 0 \quad , \tag{1}$$

$$\frac{\partial u_i}{\partial t} + u_j \frac{\partial u_i}{\partial x_j} = -\delta_{i3}\frac{\Pi}{\rho} - \frac{1}{\rho}\frac{\partial p}{\partial x_i} + \nu \frac{\partial^2 u_i}{\partial x_j^2} \quad , \tag{2}$$

where u_i, ρ, and p represent the velocity, density and pressure of the fluid, respectively. Following the convention of tensor notation, coordinates (x, y, z) and velocities (u, v, w) are also denoted as (x_1, x_2, x_3) and (u_1, u_2, u_3), respectively. The flow is driven by a constant mean pressure gradient Π, and δ_{i3} is the Kronecker delta. The flow is fully developed, with a periodic boundary condition applied to the streamwise direction, and a no-slip condition enforced on all solid walls.

The DNS was performed using a spectral-element code called "Semtex" developed by Blackburn and Sherwin (2019), which has a spectral accuracy and is highly suitable for conducting rigorous DNS. The code is written in the C/C++ and FORTRAN coding languages and is made parallel using message passing interface (MPI) standard. The x-y plane of the mesh was constructed out of four identical isosceles trapezoids, each containing 99 quadrilateral finite elements. An 8th-order Guass-Labatto-Legendre Lagrange polynomial was used for further spatial discretization within each finite element, and 2048 Fourier modes were applied to the homogeneous z-direction. The grid spacing in the x- and y-directions ranges from $\Delta x^+ = 1$ to 5, and the spacing in the z-direction is uniform ranging from $\Delta z^+ = 11$ to 25.

Table 1: Geometry and flow parameters of the test cases.

Test case	D/d	Re_τ	Re_b	$\langle w\rangle^+_{max}$	f
C1	3	240	3532	17.95	0.037
C2	3	430	6991	19.05	0.031
C3	3	600	10489	20.37	0.026
XP	2	200	3058	18.69	0.034

For each simulated case, at least 600 instantaneous flow fields were collected over at least 45 large-eddy turnover times (LETOTs, defined as h/u_τ). In the analysis, the instantaneous velocity is decomposed as $u = \langle u\rangle + u'$, where $\langle\cdot\rangle$ represents averaging over time and over the homogeneous z-direction, and $(\cdot)'$ represents fluctuations from the mean. In result analysis, variables expressed in wall coordinates (denoted using superscript '+') were calculated based on the average wall friction velocity defined as $u^a_\tau = \sqrt{\tau^a_w/\rho}$, where the surface-averaged wall shear stress is determined as (Bagheri *et al.,* 2020)

$$\tau^a_w = \frac{A_i \tau^a_{wi} + A_o \tau^a_{wo}}{A_i + A_o} \quad . \tag{3}$$

In the above equation, $A_i = 4dL_z$ and $A_o = 4DL_z$ are the surface areas of the inner and outer ducts, respectively. The average wall shear stresses at the inner and outer duct walls are defined as $\tau^a_{wi} = \int_P \tau_{wi} dl/P$ and $\tau^a_{wo} = \int_P \tau_{wo} dl/P$, respectively, where $P = 4d$ or $4D$ is the perimeter of the inner and outer duct. Also, $\tau_{wi} = \rho\nu\partial\langle w\rangle/\partial n$ and $\tau_{wo} = -\rho\nu\partial\langle w\rangle/\partial n$ are the local streamwise-averaged wall shear stresses at the inner and outer duct walls, respectively, where n denotes the wall-normal coordinate (either x or y). All simulations and data storage are executed on the Grex supercomputer located at the University of Manitoba.

RESULTS AND DISCUSSION

Table 1 summarizes the key flow parameters of the three test cases along with those of the DNS study of Xu and Pollard (2008), denoted here as 'XP' and cited for the purpose of comparison. Here, $Re_\tau = hu^a_\tau/\nu$ is the friction Reynolds number, $\langle w\rangle^+_{max}$ is the maximum mean streamwise velocity and $f = 8(u^a_\tau/W_b)^2$ is the friction factor. From Table 1, it can be seen that the friction factor decreases from $f = 0.037$ to 0.026 for case C1 to C3. The result of case C1 is comparable to that of XP at a similar Reynolds number. It is interesting to note that $\langle w\rangle^+_{max}$ is located between the inner and outer walls for the lower Reynolds number cases C1 and XP. In stark contrast, $\langle w\rangle^+_{max}$ is located along the corner bisector for C2 and C3. This indicates that as the Reynolds number increases, the secondary flows induced by the convex and concave corners act to transfer momentum away from the WBS and to the CBS. It is also worth noting that as the Reynolds number increases from $Re_b = 7000$ to 10500, the location of $\langle w\rangle^+_{max}$ shifts along the CBS towards the concave corner of the outer duct.

Figure 2 presents the contours of the mean streamwise velocity $\langle w\rangle$ non-dimensionalized by the bulk velocity W_b for cases C1, C2 and C3, superimposed with the streamlines in the cross-stream direction. Due to the symmetry of the flow domain, only the bottom left corner is displayed for each case. As shown in Figure 2(a), there exists 2 counter-rotating vortex pairs centered along the CBS in case C1. One of the pairs is

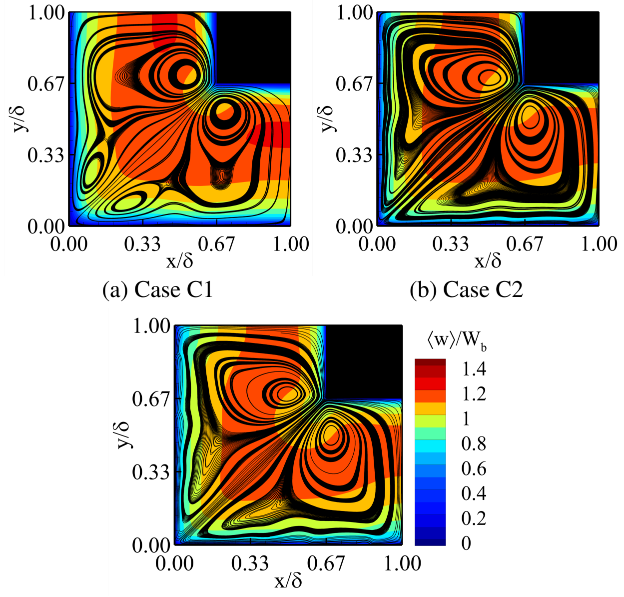

(a) Case C1 (b) Case C2

(c) Case C3

Figure 2: Contours of the non-dimensional mean streamwise velocity $\langle w\rangle/W_b$ superimposed with streamlines in a cross-stream plane. Due to the symmetry of the mean flow field, only the bottom left corner of the concentric duct is displayed for each case.

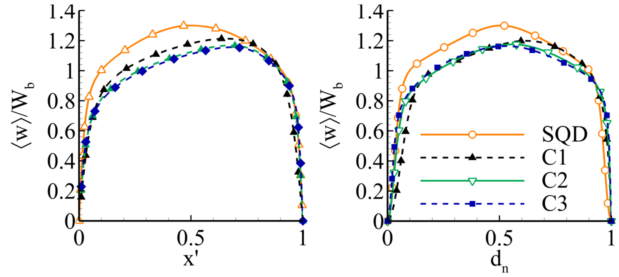

(a) WBS (b) CBS

Figure 3: Profiles of the mean streamwise velocity $\langle w\rangle/W_b$ along the WBS and CBS.

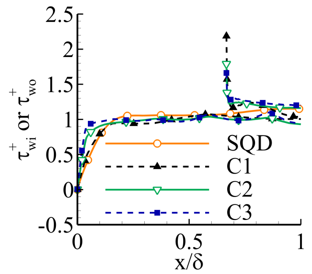

Figure 4: Profiles of the wall shear stresses along the inner and outer bottom walls (τ^+_{wi} and τ^+_{wo}, respectively).

focused near the outer concave corner while the other is focused around the inner convex corner. This secondary flow pattern was also observed by Xu and Pollard (2009). By contrast, as shown in Figures 2(b) and (c), it is interesting to note that the vortex pair commonly associated with streamwise turbulent flow along a concave corner vanishes at relatively higher Reynolds numbers. By comparing Figures 2(a)-(c), it is observed that the convex corner contributes increasingly to the generation of secondary flow as the Reynolds number increases. This suggests that as the flow rate increases, the secondary flows generated by the inner convex corner eventually become strong enough to overpower the vortex pair generated by the concave corner.

Figure 3 presents profiles for the mean streamwise velocity $\langle w\rangle/W_b$ along the WBS and CBS. In the annular duct cases, the profiles along the CBS span from the bottom left concave outer corner to the bottom left convex inner corner. By contrast, in a single smooth square duct (SQD) flow case, the profiles along the diagonal line span from the bottom left concave corner to the top right concave corner. From the profiles along the WBS shown in Figure 3(a), it is evident that the gradient at the inner wall ($x' = 1.0$) increases monotonically with Re_b. Turning our attention to Figure 3(b), it is shown clearly that the peak value of $\langle w\rangle/W_b$ shifts towards the concave corner as the Reynolds number increases. Clearly, the velocity profile approaches the convex corner differently than it approaches the concave corner. Specifically, the profile of $\langle w\rangle$ expresses a zero gradient at $d_n = 0$ due to the damping in the concave corner, while the mean velocity increases abruptly at $d_n = 1.0$ due to the flow enhancement in the convex corner.

The profiles of the average wall shear stresses τ^+_{wi} and τ^+_{wo} (non-dimensionalized by u^a_τ and ρ) along the bottom inner and outer walls are displayed in Figure 4. The profiles along the outer wall in the region of the concave corner increase more rapidly as the Reynolds number increases. Moving along the x-direction, the profiles of the average wall shear stresses in the annular duct cases are comparable to that of the smooth square duct, and only begin to diverge when the WBS is reached ($x/\delta = 1.0$). This is consistent with the profiles of the mean velocity in Figure 3, which show decreased velocity gradients at the WBS for all three annular duct cases. Unlike the concave corner at $x/\delta = 0.0$, the average wall shear stress is non-zero at the convex corner of the inner duct and shows a sharp change in range $0.67 \le x/\delta \le 0.69$. At the convex corner, the wall shear stress is $\tau^+_{wi} = 2.186$, 1.791 and 1.661 for cases C1, C2, and C3, respectively.

Figure 5 presents horizontal profiles of the mean viscous $\tau_{visc} = \nu\,(\partial\langle w\rangle/\partial x + \partial\langle w\rangle/\partial y)$, turbulent $\tau_{turb} = -\left(\langle u'w'\rangle + \langle v'w'\rangle\right)$ and total $\tau_{tot} = \tau_{visc} + \tau_{turb}$ shear stress across the annular gap along the WBS and CBS. From Figures 5(a), it is seen that along the WBS, the profiles of cases C2 and C3 closely resemble that of the SQD case. Meanwhile, the profile of case C1 deviates slightly within a distance of $\Delta y/\delta = 0.2$ from both the outer and inner walls. Similar to the profiles shown in Figure 4, the viscous shear stress near the outer WBS and the convex corner reduces as the Reynolds number increases. This trend is attributed the fact that as the Reynolds number increases, the secondary flow strengthens (as seen in Figure 2) which acts to transfer momentum away from the outer WBS and inner CBS. In effect, this reduces the velocity gradient at the outer WBS and the inner CBS, and thus reduces the viscous shear stress at these locations. This line of reasoning was also used by Prandtl (1926) to explain the migration of $\langle w\rangle^+_{max}$ into the concave corner. Figures 5(c) and (d) show the Reynolds stress profiles τ^+_{turb} along the WBS and CBS, respectively. It can be seen that the region in which the profiles are linear is limited for all annular duct cases in contrast to the SQD case. The total shear stress along the WBS and CBS is presented in Figures 5(e) and (f), respectively.

The contours of the mean turbulence kinetic energy $k^+ = \langle u'_i u'_i\rangle/2\,(u^a_\tau)^2$ for cases C1, C2 and C3 are presented in Figures 6(a), (b) and (c), respectively. The contours reveal that the TKE is significant near the inner and outer walls, with dampened regions near the concave corners, and an enhanced 'bulb' around the convex corner in all three annular duct cases. As the

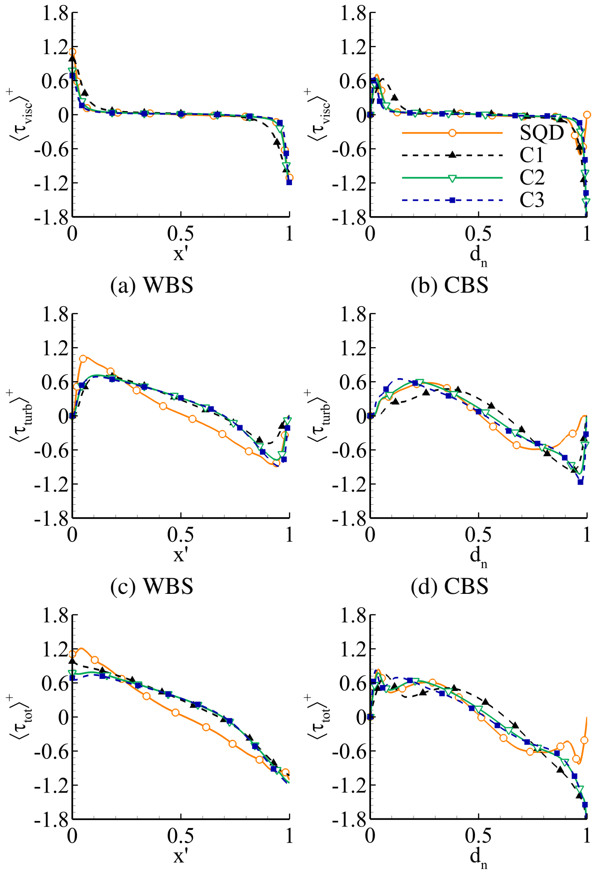

(a) WBS (b) CBS
(c) WBS (d) CBS
(e) WBS (f) CBS

Figure 5: Profiles of the viscous, Reynolds and total shear stress across the gap of the annulus along the WBS and CBS.

Reynolds number increases, this 'bulb' shrinks while values of k^+ enhance greatly close to the entire inner wall. Additionally, the region of dampened TKE in the concave corner reduces monotonically from cases C1 to C3. Qualitatively, the contour patterns of k^+ in the WBS region are similar to those of a plane channel flow, while the values of k^+ along the CBS are greatly augmented.

Figures 7(a) and (b) further present the profiles of k^+ along the WBS and CBS, respectively. From Figure 7(a), it is seen that the minimum value of TKE is similar in all test cases with $k^+ \approx 0.8$, occurring at $x' \approx 0.5$ in the SQD case, but at $x' \approx 0.65$ in the three annular duct cases. Turning our attention to the CBS presented in Figure 7(b), it is seen that the profiles for the annular duct flows are very different from those of the SQD case. From these profiles, it is seen that as the Reynolds number increases, the TKE level enhances near both the inner and outer corners. It is interesting to observe that although the profiles of the TKE along the CBS change significantly with Reynolds number, the location of the maximum value remains relatively stable near both the concave and convex corners. Near the concave outer corner, the peak occurs at a distance of $\Delta d_n \approx 0.1$ from the wall. By contrast, the peak near the convex inner corner occurs at a distance of $\Delta d_n \approx 0.04$ from the wall.

The transport equation for the TKE is given by

$$0 = H_k + P_k + \varepsilon_k + D_k^t + D_k^p + D_k^v \quad , \tag{4}$$

where H_k, P_k, ε_k are the convection, production and dissipation terms, respectively. The TKE diffusion is broken up into the turbulent, pressure and viscous components, denoted by

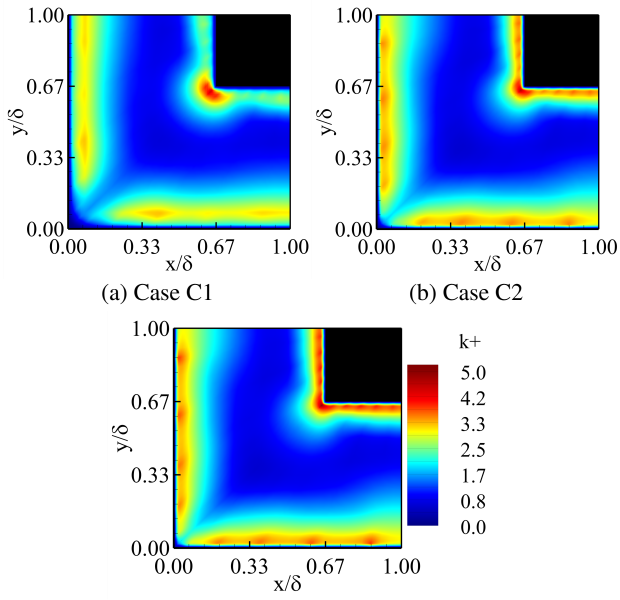
(a) Case C1 (b) Case C2
(c) Case C3

Figure 6: Contours of the non-dimensionalized TKE k^+.

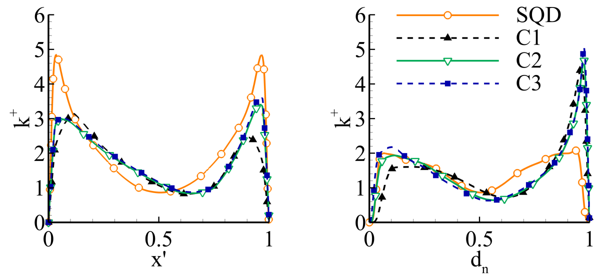

(a) WBS (b) CBS

Figure 7: Profiles of the non-dimensionalized TKE k^+ across the gap of the annulus along the WBS and CBS.

D_k^t, D_k^p and D_k^v, respectively. The budget balance of the TKE transport equation across the annular gap along the WBS and CBS are presented in Figure 8. For all four test cases, the profiles are qualitatively similar in the sense that the production (P_k) and dissipation (ε_k) act as the main source and sink terms, respectively. Additionally, along the WBS of all four of the test cases, the dissipation (ε_k) and viscous diffusion (D_k^v) are the main source and sink terms at the inner and outer walls. A comparison of Figures 8(c), (e) and (g) shows that as the Reynolds number increases, the magnitude of the production peak increases monotonically. Along the CBS, the profiles behave similar to those along the WBS in the core region, but differ in the near-wall regions. For all four test cases, all the budget terms fall to zero as the concave corner is approached. Near the convex corner, the convection (H_k) is greatly enhanced compared to other locations, and is seen to increase in strength as the Reynolds number increases from case C1 to C3. At the convex corner, the dissipation and viscous diffusion terms increase dramatically compared to the inner WBS region.

Figure 9 displays the isopleths of the 1-D pre-multiplied energy spectra $k_z^+ \phi_k^+$ of all four test cases. Here, k_z^+ denotes the streamwise wave number and $\lambda_z^+ = 2\pi/k_z^+$ represents the streamwise wavelength non-dimensionalized by u_τ^a and δ. The yellow star symbol '*' indicates the peak location of the pre-multiplied spectrum, i.e. $(k_z^+ \phi_k^+)_{max}$. Figures 9(a), (c), (e)

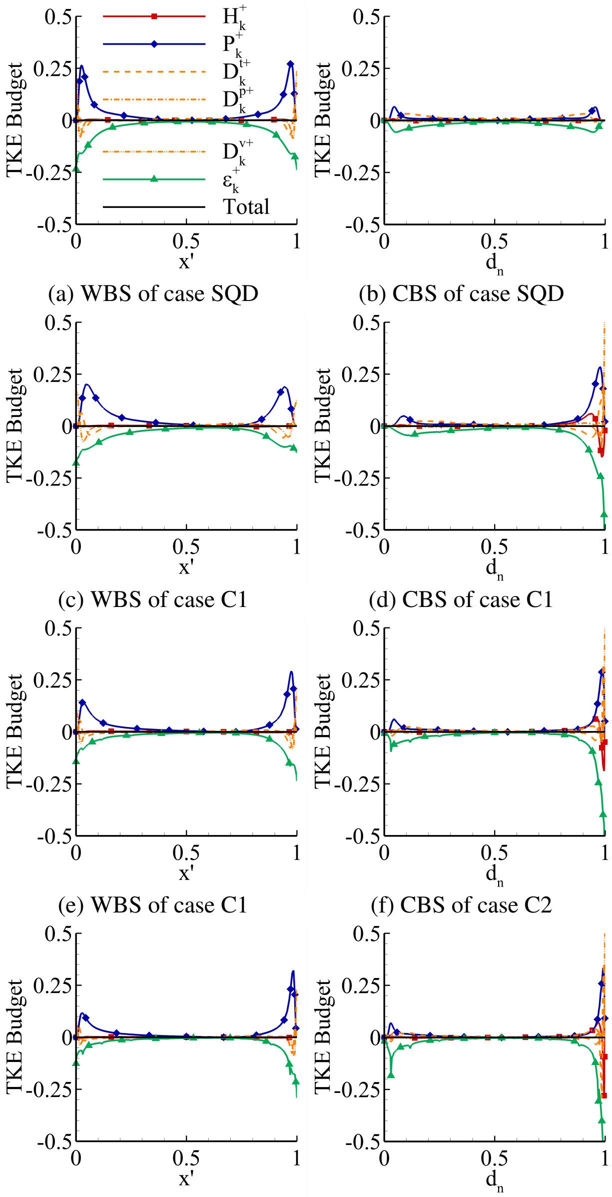

(a) WBS of case SQD (b) CBS of case SQD

(c) WBS of case C1 (d) CBS of case C1

(e) WBS of case C1 (f) CBS of case C2

(g) WBS of case C3 (h) CBS of case C3

Figure 8: Profiles of the budget balance terms of the TKE transport equation along the WBS and the CBS for all four test cases.

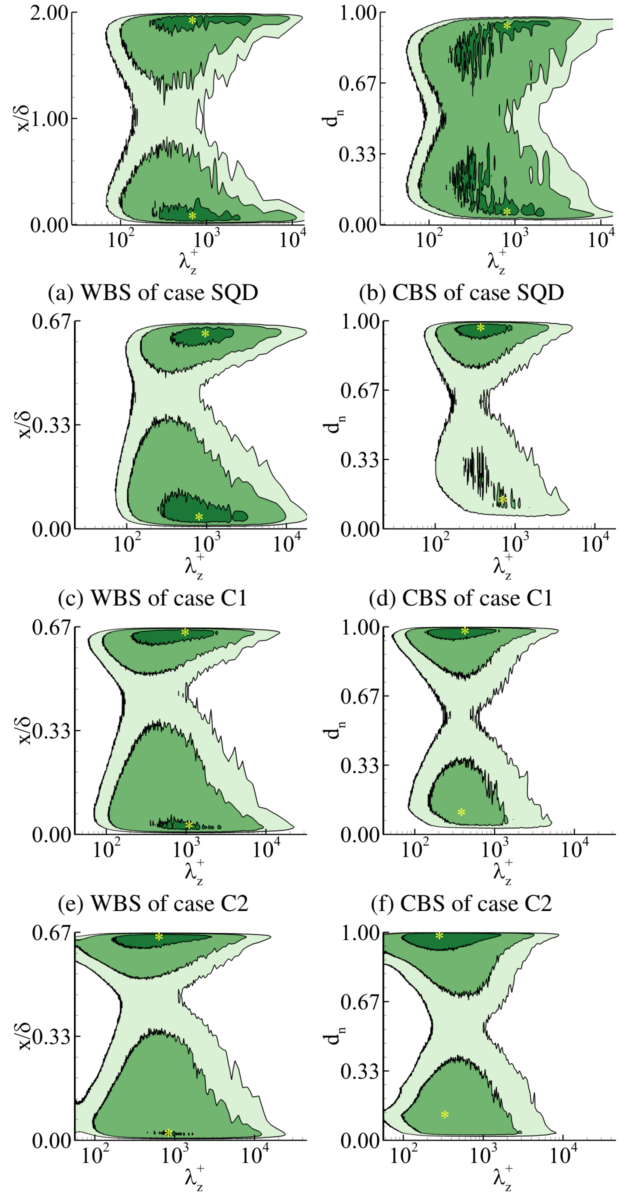

(a) WBS of case SQD (b) CBS of case SQD

(c) WBS of case C1 (d) CBS of case C1

(e) WBS of case C2 (f) CBS of case C2

(g) WBS of case C3 (h) CBS of case C3

Figure 9: Isopleths of the 1-D pre-multiplied energy spectra $k_z^+\phi_k^+$ along the WBS and CBS with respect to the streamwise wavelength λ_3^+. Three energy levels are plotted which correspond to 62.5%, 25% and 12.5% of $(k_z^+\phi_k^+)_{max}$. The yellow star symbol '*' denotes the location of the peak value $(k_z^+\phi_k^+)_{max}$.

and (g) present the isopleths along the WBS in the $x/\delta-\lambda_z^+$ plane, while Figures 9(b), (d), (f) and (h) present the isopleths along the CBS in the $d_n-\lambda_z^+$ plane. In Figure 9, the three isopleth levels are defined by 62.5%, 25% and 12.5% of $(k_z^+\phi_k^+)_{max}$. The energy for the SQD case peaks at a distance of $\Delta y^+ \approx 13.5$ along the WBS. In all annular duct flow cases, there are two energy peaks, one near the inner duct and one near the outer duct. The energy peak is always greatest near the inner duct compared to the outer duct. The location of $(k_z^+\phi_k^+)_{max}$ near the inner WBS is $x/\delta = 0.622$, 0.647, 0.653 for cases C1, C2 and C3, respectively. For the outer WBS, the location of $(k_z^+\phi_k^+)_{max}$ occurs at $x/\delta = 0.039$, 0.023, 0.021 for cases C1, C2 and C3, respectively. Clearly, as the Reynolds number increases, the inner and outer energy peaks along the WBS migrate towards their respective walls. This is in agreement with the TKE profiles along the WBS presented in Figure 7(a) earlier where the peak values of TKE shifted towards the walls as the flow rate increases. The plots show that the wavelength associated with $(k_z^+\phi_k^+)_{max}$ near the inner WBS decreases from $\lambda_z^+ = 1000$ to 600 as the Reynolds number increases from $Re_b = 3532$ to 10489. Meanwhile, the wavelength for $\max(k_z^+\phi_k^+)$ at the outer WBS increases from $\lambda_z^+ \approx 800$ to 1000 as the Reynolds number increases. Along the CBS, it is observed that the location of $(k_z^+\phi_k^+)_{max}$ away from the walls remains unchanged from case C1 to C3. Again, this is in agreement with the TKE profiles along the CBS presented in Figure 7(b) that the peak values of TKE were shown to be independent of the Reynolds number. From Figure 9, it is observed that the wavelengths corresponding to $(k_z^+\phi_k^+)_{max}$ near the inner CBS decreases from $\lambda_z^+ \approx 400$ to 300. Meanwhile, the wavelength for $(k_z^+\phi_k^+)_{max}$ at the outer CBS decreases from $\lambda_z^+ \approx 600$ to 300. From Figure 9, it is observed that as the Reynolds number increases, the range of relevant

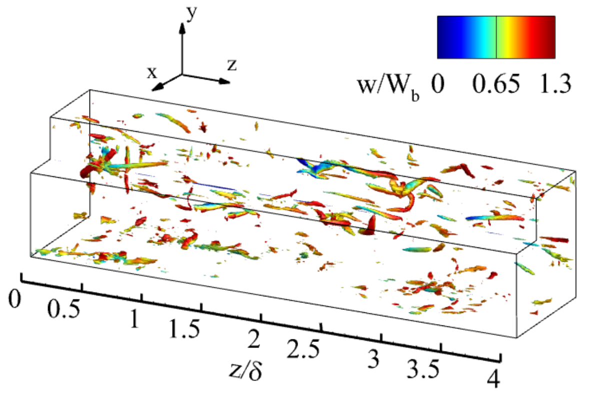

(a) Case C1

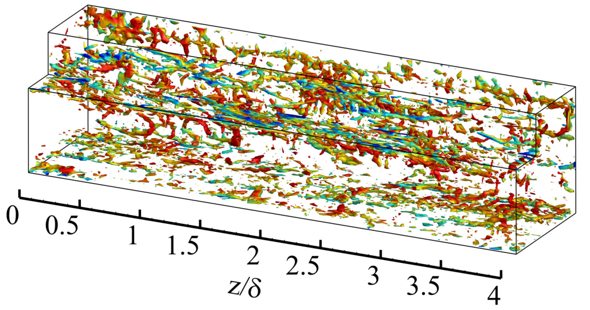

(b) Case C2

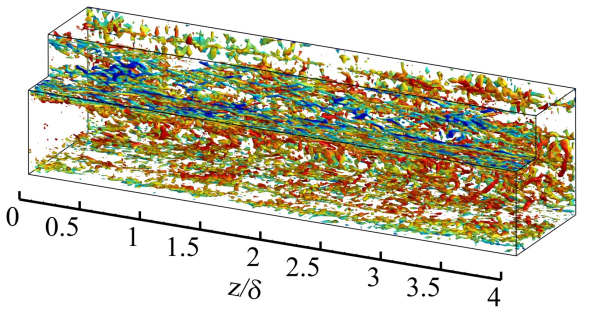

(c) Case C3

Figure 10: Vortex structures for each of the annular duct flows visualized using swirling strength λ_{ci} colored with the instantaneous non-dimensionalized streamwise velocity w/W_b. The swirling strength for all of the cases was set to $\lambda_{ci} = 5$.

wavelengths expands to include smaller length scales in both WBS and CBS planes. Notably, a small amount of energy (12.5% and 25% of the peak value) is not contained in the plot of Figures 9(e) and (f). This suggests that at the highest Reynolds number tested ($Re_b = 10500$) in case C3, the smallest energetically relevant length scales along WBS and CBS planes are not fully captured. The grid resolution will need to be increased to capture the smallest scale velocity fluctuations at this high Reynolds number.

Figures 10(a), (b) and (c) compare the vortex structures of cases C1, C2 and C3, respectively, in the lower left quarter of the domain. For clarity, only a partial streamwise domain of $0 \leq z/\delta \leq 4$ is displayed for each case. The coherent structures are visualized using the instantaneous swirling strength (λ_{ci}) non-dimensionalized using W_b and δ, further colored by the instantaneous non-dimensional velocity w/W_b. To allow for a meaningful comparison, the structures are visualized by setting $\lambda_{ci}\delta/W_b = 5$ for all three annular duct cases. It is seen that the structures for all test cases are clustered near the inner and outer walls of the annular square duct. Additionally, it is observed that the structures are more heavily concentrated near the convex corners. It is clear that as the Reynolds number increases, the density of the flow structures becomes greatly increased.

CONCLUSION

Direct numerical simulations of fully-developed turbulent flow through a concentric annular square duct have been performed to investigate the Reynolds number effects on the statistical moments of the velocity field and vortex structures. In order to identify the Reynolds number effects, three Reynolds numbers of $Re_b = 3500$, 7000 and 10500 were compared. Additionally, a square duct flow of $Re_b = 3500$ was performed as a baseline case for comparison.

The friction factor f in the annular duct is seen to decrease monotonically as the Reynolds number increases. Due to the presence of the four additional convex corners, the secondary flows of a concentric annular duct flow are considerably more complex than those of a smooth duct flow. It is observed that the peak position of the mean streamwise velocity moves from the region of the wall bisector to the region of the corner bisector as the Reynolds number increases. The secondary flows are strengthened at higher Reynolds numbers and act to transfer momentum from the wall bisector towards the concave corner. Furthermore, at higher Reynolds numbers, the vortex pair near the concave corner disappeared. The location of the peak TKE value along the CBS was shown to be independent of Reynolds number. The plots of the 1-D pre-multiplied energy spectra $k_z^+\phi_k^+$ concluded that as the Reynolds number increases, the characteristic length of the coherent structures increases along the outer WBS, but decreases along the inner WBS and the concave and convex corners. A visualization of turbulence structures using the swirling strength λ_{ci} showed the coherent structures congregate near the duct walls and corners, which become increasingly populated with vortexes as Reynolds number increases.

REFERENCES

Bagheri, E., Wang, B.-C. & Yang, Z. 2020 Influence of domain size on direct numerical simulation of turbulent flow in a moderately curved concentric annular pipe. *Phys. Fluids* **32**(6), 065105.

Blackburn, H.M., Lee, D., Albrecht T. & Singh, J. 2019 Semtex: a spectral element Fourier solver for the incompressible Navier-Stokes equations in cylindrical or Cartesian coordinates. *Comput. Phys. Commun.* **140**, 27-44.

Bradshaw, P. 1987 Turbulent secondary flows. *Ann. Rev. Fluid Mech.* **19**, 53-74.

Huser, A., Biringen, S. & Hatay, F. 1993 Direct simulation of turbulent flow in a square duct: Reynolds-stress budgets. *Phys. Fluids* **6**(9), 3144-3152.

Prandtl, L. 1926 Uber die ausgebildete turbulenz. *Verh. 2nd Intl. Kong. Fur Tech. Mech., Zurich* [English translation NACA Tech. Memo. 435, 62].

Wang, D., Li, H., Li, Y., Yu, T & Xu, H. 2019 Direct numerical simulation and in-depth analysis of thermal turbulence in square annular duct. *Int. J. Heat Mass Trans.* **114**, 118590.

Xu, H. 2009 Direct numerical simulation of turbulence in a square annular duct. *J. Fluid. Mech.* **621**, 23-57.

Xu, H. & Pollard, A. 2001 Large eddy simulation of turbulent flow in a square annular duct. *Phys. Fluids* **13**(11), 3321-3337.